

Absolute orientation-dependent anisotropic TiN(111) island step energies and stiffnesses from shape fluctuation analyses

S. Kodambaka, S. V. Khare, V. Petrova, D. D. Johnson, I. Petrov, and J. E. Greene

Department of Materials Science and the Frederick Seitz Materials Research Laboratory, University of Illinois, 104 South Goodwin Avenue, Urbana, Illinois 61801

(Received 15 August 2002; published 16 January 2003)

In situ high-temperature (1165–1248 K) scanning-tunneling microscopy was used to measure temporal fluctuations about the anisotropic equilibrium shape of two-dimensional TiN(111) adatom and vacancy islands on atomically smooth TiN(111) terraces. The equilibrium island shape was found to be a truncated hexagon bounded by alternating $\langle 110 \rangle$ steps, which form $[100]$ and $[110]$ nanofacets with the terrace. Relative step energies β as a function of step orientation φ were obtained from the inverse Legendre transformation of the equilibrium island shape to within an orientation-independent scale factor λ , the equilibrium chemical potential of the island per unit TiN area. We find that for alternating S_1 and S_2 $\langle 110 \rangle$ steps, the ratio $\beta_1/\beta_2=0.72 \pm 0.02$. The parameter λ and, hence, absolute orientation-dependent values of $\beta(\varphi)$ and step stiffnesses $\tilde{\beta}(\varphi)$ were extracted from quantitative shape fluctuation data using an exact theoretical approach valid for anisotropic islands. For the two $\langle 110 \rangle$ steps, we obtain $\beta_1=0.23 \pm 0.05$ and $\tilde{\beta}_1=1.9 \pm 1.1$ eV/Å with $\beta_2=0.33 \pm 0.07$ and $\tilde{\beta}_2=0.08 \pm 0.02$ eV/Å over the observed temperature range. Due to the correspondingly high kink energies, TiN(111) step energies exhibit only a very weak temperature dependence between 0 K and the maximum measurement temperature 1248 K.

DOI: 10.1103/PhysRevB.67.035409

PACS number(s): 68.35.Md, 68.35.Ja, 68.37.Ef, 82.45.Mp

I. INTRODUCTION

NaCl-structure TiN is widely used as a hard wear-resistant coating on cutting tools, as a diffusion-barrier layer in microelectronic devices, as a corrosion-resistant coating on mechanical components, and as an abrasion-resistant layer on optics and architectural glass. Even though the elastic and diffusion-barrier properties of TiN are highly anisotropic, and hence depend strongly upon film texture, the mechanisms and reaction paths leading to the development of preferred orientation in polycrystalline TiN layers are not understood. Efforts to model these processes require, as input, detailed knowledge of adatom transport and surface site energies.¹ Relatively little information is available concerning these parameters although, recently, some progress has been made toward obtaining adatom transport activation energies on TiN(001) and (111) surfaces.² Here, we focus on the determination of absolute orientation-dependent step formation energies and stiffnesses on TiN(111).

The step formation energy β as a function of step orientation φ is a fundamental parameter used to describe crystal surfaces. $\beta(\varphi)$ is the two-dimensional (2D) analog of the surface free energy $\gamma(\hat{\mathbf{n}})$, where $\hat{\mathbf{n}}$ is a unit vector normal representing a facet orientation. Just as $\gamma(\hat{\mathbf{n}})$ determines the equilibrium shape of bulk crystals, the variation of β with φ determines the equilibrium shape of 2D islands on a terrace. A related property, the step-edge stiffness $\tilde{\beta}(\varphi)$, defined as

$$\tilde{\beta}(\varphi) \equiv \beta(\varphi) + d^2\beta(\varphi)/d\varphi^2, \quad (1)$$

is proportional to the island chemical potential,³ and hence controls island coarsening and decay kinetics. Unfortunately, very little data, either experimental or theoretical, is avail-

able concerning $\beta(\varphi)$ and $\tilde{\beta}(\varphi)$, even for elemental metal surfaces.⁴

Experimental determination of absolute orientation-dependent step energies is difficult. An “inverse” Wulff plot^{5,6} constructed from direct measurements of the equilibrium shape of 2D islands yields only the *relative* orientation dependence of step energies. Additional experiments are necessary to determine *absolute* values of $\beta(\varphi)$. Bartelt, Tromp, and Williams⁷ used step fluctuation measurements for Si(001), while Bonzel and co-workers⁸ employed 3D equilibrium crystal shape measurements and surface energies for Pb(111). Icking-Konert, Geisen, and Ibach⁹ described a method for determining absolute β values from the temperature dependence of Cu(100) equilibrium island shapes. This approach was also used to obtain β along the two $\langle 110 \rangle$ steps on Pb(111).¹⁰ *Orientation-averaged* step energies have been extracted from 2D island coarsening measurements.^{2,11,12} Recently, a method to determine absolute $\beta(\varphi)$ values from a combination of 2D island coarsening and equilibrium island shape measurements was derived and applied to TiN(001).¹³ Schlößer *et al.*¹⁴ have shown, in an extension of existing island shape fluctuation theory,¹⁵ that fluctuation measurements of nearly isotropic island shapes at a single temperature can be used to determine absolute *average* step energies. Steimer *et al.*¹⁶ found that the average Cu(100) and Ag(100) step energies determined using this procedure were in good agreement with the results obtained from the method described in Ref. 9. This technique, however, is not suitable for obtaining $\beta(\varphi)$ for anisotropic island shapes.

We have recently developed an approach, applicable to both isotropic and highly anisotropic islands, for the determination of orientation-dependent step energies from shape fluctuation measurements.^{17,18} In this paper, we present *in situ* high-temperature (1165–1248 K) scanning-tunneling

microscopy (STM) measurements of temporal fluctuations about the anisotropic TiN(111) equilibrium shape of two-dimensional adatom and vacancy islands on atomically smooth TiN(111) terraces. The root mean square of these fluctuation amplitudes is anisotropic with a threefold symmetry coinciding with that of the equilibrium shape. We analyze the data using the shape fluctuation theory for anisotropic islands described in Refs. 17 and 18 and hence determine absolute values of $\beta(\varphi)$ and $\bar{\beta}(\varphi)$. For the two $\langle 110 \rangle$ steps, S_1 and S_2 , we also obtain kink energies ε_1 and ε_2 .

II. EXPERIMENTAL PROCEDURE

Epitaxial TiN(111) layers, 2000-Å thick, were grown on polished $9 \times 2 \times 0.5$ -mm³ Al₂O₃(11 $\bar{2}$ 0) substrates at $T_s = 1050$ K in a load-locked multichamber ultrahigh vacuum (UHV) system by magnetically unbalanced dc magnetron sputter deposition¹⁹ using the procedure described in Ref. 20. The pressure in the sample introduction chamber was reduced to 5×10^{-8} Torr using a 50-l/s turbomolecular pump (TMP) before initiating substrate exchange with the main chamber, which had a base pressure of 10^{-10} Torr, achieved using a 500-l/s TMP. The 7.62-cm-diameter water-cooled Ti target (99.999% purity) was sputtered at a constant power of 90 W in pure N₂ (99.999%) discharges at a total pressure of 5×10^{-3} Torr.

Substrate cleaning consisted of successive rinses in ultrasonic baths of trichloroethane, acetone, methanol, and deionized water. The wafers were then blown dry with dry N₂, mounted on resistively heated Ta platens using Mo clips, and inserted into the sample introduction chamber for transport to the growth chamber. The Al₂O₃ substrates were thermally degassed for 12 h at 1200 K with the growth chamber at 350 K. Prior to initiating deposition, the chamber was water cooled to room temperature, the substrate temperature lowered to 1050 K, and the target sputter etched for 5 min with a shutter shielding the substrate. Sample temperatures were measured by optical pyrometry and calibrated using temperature-dependent TiN emissivity data obtained by spectroscopic ellipsometry. Postdeposition Rutherford backscattering spectroscopy measurements, analyzed using the RUMP computer-simulation program,²¹ showed that the layers were stoichiometric with a N/Ti ratio of 1.02 ± 0.02 .

The TiN(111)/Al₂O₃(11 $\bar{2}$ 0) samples were transferred to a UHV multichamber system, with a base pressure of 2×10^{-10} Torr, containing a variable-temperature Omicron scanning-tunneling microscope. The system was also equipped with facilities for residual gas analysis, electron-beam evaporation, ion etching, Auger electron spectroscopy, and low-energy electron diffraction (LEED). The TiN layers were degassed in the STM sample preparation chamber at 1073 K, where the vapor pressure of N₂ over TiN was less than 10^{-10} Torr,²² for approximately 20 min. Epitaxial TiN(111) buffer layers, 50–100-Å thick, were deposited at 1023 K by reactive evaporation from Ti rods (99.999% purity) at a deposition rate of ≈ 0.025 ML/s in 1×10^{-7} -Torr N₂ (99.999%) and annealed in N₂ for 4 h at temperatures $T_a \approx 1100$ K. This procedure resulted in sharp 1×1 LEED

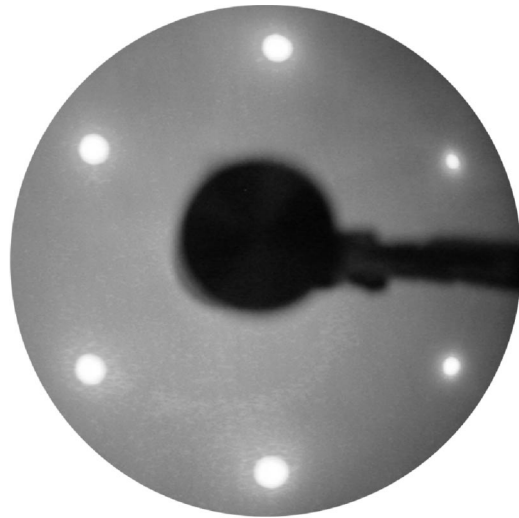


FIG. 1. Typical LEED pattern, obtained at 200 V, from a TiN(111) buffer layer grown at $T_s = 1100$ K.

patterns corresponding to an in-plane atomic spacing of 2.99 Å and an STM-measured step height of 2.4 Å, both equal to expected values for bulk-terminated TiN(111).²³ A typical LEED pattern is shown in Fig. 1. AES analyses indicated that the samples contained ≈ 2 -mole % oxygen, probably in the form of TiO, which is isostructural²³ and mutually soluble with TiN. STM images reveal ≈ 500 -Å-wide atomically smooth terraces separated by bilayer-height (≈ 2.4 -Å) steps.²⁴

TiN(111) partial bilayers (BL) with coverages of 0.1–0.8 BL were deposited on TiN(111) buffer layers by reactive evaporation at room temperature. The samples were then annealed *in situ* at $T_a = 1165$ –1248 K in 1×10^{-7} -Torr N₂ for $t_a = 1$ –2 h. This procedure resulted in 2D TiN(111) adatom islands for coverages < 0.4 BL and vacancy islands at higher coverages. Both the terraces and the islands were expected to be N terminated, the lowest-energy TiN(111) surface.²⁵ The results presented here correspond to STM measurements of adatom and vacancy islands with average radii ranging from 50 to 260 Å.

At each sample annealing temperature T_a , STM images (typically 50 per sequence) were acquired as a function of annealing time t_a at a constant rate (18–44 s/frame). Typical tunneling conditions were 0.4–0.6 nA at -3.5 V. The sample and tip were allowed to stabilize thermally at T_a for 2–3 h prior to obtaining the STM images. Thermal drift in the scans, typically 1 Å/s, was periodically corrected in order to sequentially acquire STM images of the same area. Pixel resolution in the images varied from 1.25×1.25 to 2.5×2.5 Å². Scan sizes, scan rates, and tunneling parameters were varied to check for tip-induced effects. No such effects were observed in the results presented here.

STM images were analyzed using IMAGE SXM,²⁶ an image processing software package, to detect island boundaries, determine island centers of mass, and measure island areas. Ostwald ripening, leading to island coarsening and decay,² was observed during the annealing experiments. Since analysis of island shape fluctuations requires islands of nearly con-

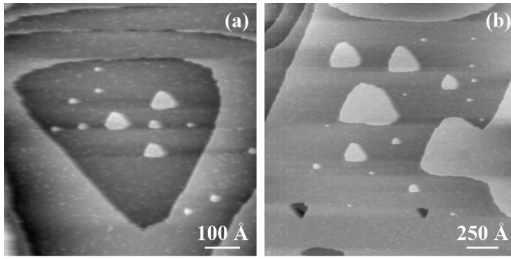


FIG. 2. Typical STM images of TiN(111) samples during annealing at temperatures T_a =(a) 1118 and (b) 1178 K. Adatom islands are light gray while vacancy islands are darker gray.

stant area,^{15,17,18} only data from consecutive scans with a maximum total change in area of $\leq 10\%$ (within the limits of image spatial resolution) were used and the boundary coordinates $r(\theta, t_a)$ of measured islands, with r and θ representing the radial and angular components, were normalized to the smallest island area in the measurement sequence. Thus, we use the island coarsening/decay phenomenon to our advantage by dividing the long-time image series into subsets, with maximum total island area changes $\leq 10\%$. With this procedure, the maximum uncertainties in step energies were estimated to be $\approx 13\%$.

III. TiN(111) EQUILIBRIUM ISLAND SHAPE ANALYSES

Figures 2(a) and 2(b) show representative STM images of TiN(111) 2D adatom (light gray) and vacancy (dark gray) islands on atomically smooth TiN(111) terraces. The images were acquired during annealing at $T_a=1118$ and 1178 K, respectively. Note that all adatom islands point in one direction while all vacancy islands point in the opposite direction. In both cases, the islands are truncated hexagons with alternating long and short steps, indicative of highly anisotropic step energies.

The NaCl-structure TiN consists of a face-centered-cubic (fcc) lattice with a two-atom, Ti and N, basis set. Figure 3(a) is a schematic illustration of a 2-BL-thick N-terminated TiN(111) terrace with both adatom and vacancy islands bounded by alternating short and long $\langle 110 \rangle$ steps. The step lengths are unequal due to a significant difference in step energies resulting from differences in local atomic arrangements. This can be seen more clearly in Fig. 3(b), which shows that the $\langle 110 \rangle$ steps form $\{100\}$ and $\{110\}$ nanofacets with respect to the terrace. [The alternating $\langle 110 \rangle$ steps bounding a simple fcc(111) surface form $\{111\}$ and $\{100\}$ nanofacets, respectively.²⁷] Due to the fcc stacking symmetry, the opposing step edges bounding both TiN(111) adatom and vacancy islands constitute of a pair of short and long steps and are oppositely directed, as shown in Fig. 3(a). Consequently, vacancy islands are rotated by 180° with respect to the adatom islands.

Figure 4 consists of two sets of three consecutive STM images each for 2D TiN(111) adatom [Fig. 4(a)] and vacancy islands [Fig. 4(b)] during annealing at 1200 K. The observed fluctuations in island shapes $r(\theta, t_a)$, as shown by the island outlines in the fourth panel of each image set, are due to thermally induced random motion of the diffusing species.

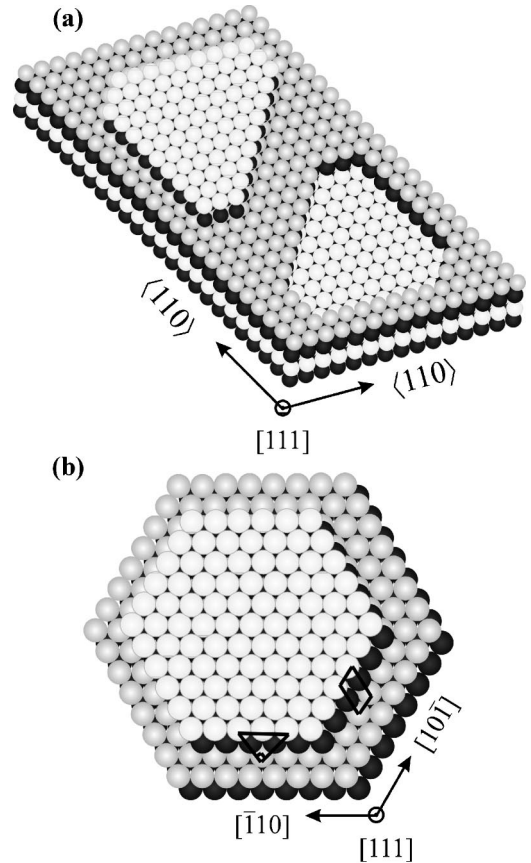


FIG. 3. Schematic illustrations showing (a) the relative orientations of 2D adatom and vacancy islands on a N-terminated two-bilayer-thick TiN(111) surface and (b) the local atomic structure of alternating step edges parallel to the close-packed $\langle 110 \rangle$ directions. The black triangle and rectangle in (b) highlight portions of $\{100\}$ and $\{110\}$ nanofacets formed by alternating $\langle 110 \rangle$ step edges with the terrace. N and Ti atoms are represented as light and dark gray spheres, respectively.

The average island shape, defined as $\bar{R}(\theta) \equiv \langle r(\theta, t_a) \rangle$, was determined from 15 to 41 consecutive images for each of 12 adatom and 14 vacancy islands of average radii 50–260 Å. Measurements were carried out at five different temperatures over the range $T_a = 1165$ –1248 K. The fluctuation kinetics were found to be identical for all adatom and vacancy islands. The results presented below are typical of all experimental data.

Figure 5(a) is a plot of $\bar{R}(\theta)$ vs θ , obtained by averaging $r(\theta, t_a)$ data from 41 images, for the vacancy island in Fig. 4(b). $\bar{R}(\theta)$ was found to be distorted, with asymmetric $\langle 110 \rangle$ step-edge lengths, due to hysteresis in the STM piezoelectric actuators.^{9,10,13} The distorted shape $\bar{R}(\theta)$ was transformed to the symmetric equilibrium island shape $R(\theta)$ using the three-fold symmetry of the TiN(111) lattice and imposing the condition $R(\theta_i + m\pi/3) \equiv (1/3) \sum_{n=0,2,4} \bar{R}(\theta_i + n\pi/3)$ for $m=0, 2, \text{ and } 4$ and θ_i values in the range 0 – $2\pi/3$. This procedure was employed only to the average island shape and not to the temporal island shapes.

The equilibrium island shape $R(\theta)$ is plotted as a function of θ in Fig. 5(b). Measured $R(\theta)$ data (open circles) were fit

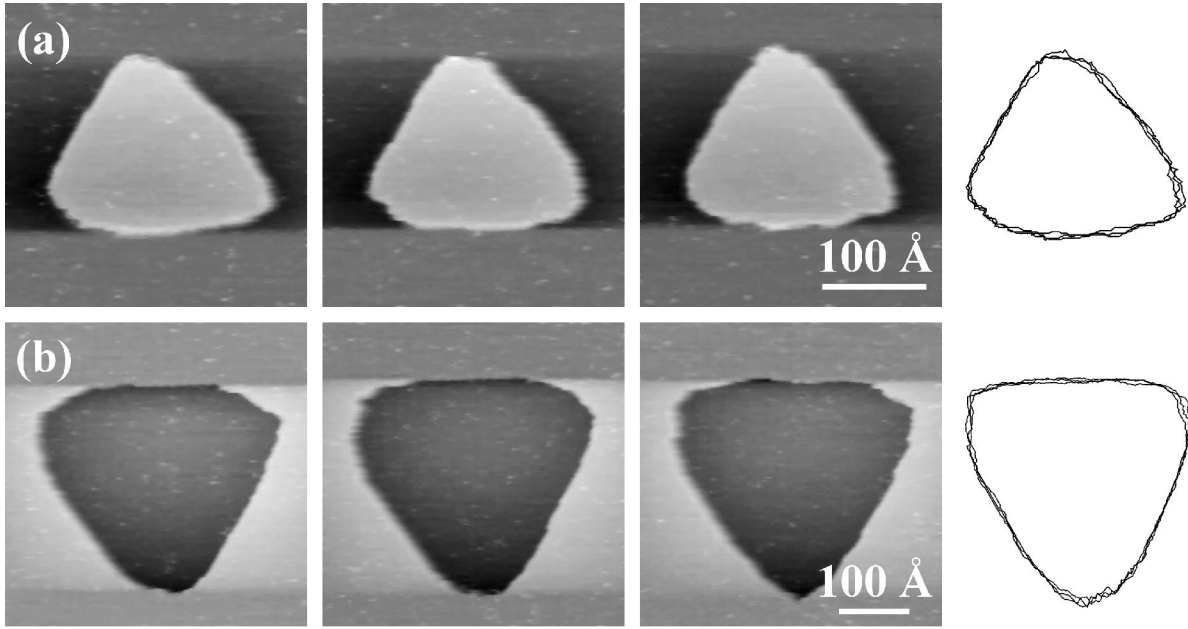


FIG. 4. Consecutive STM images of 2D TiN(111) (a) adatom and (b) vacancy islands acquired at 35 and 32 s/frame, respectively, during annealing at $T_a=1200$ K. The fourth panels in (a) and (b) are the island boundaries $r(\theta, t_a)$ from each image.

at θ values from 0 to $2\pi/3$ with two Lorentzian functions of general form,

$$R(\theta) = R_o + \frac{a}{[1 + b(\theta - \theta_c)^2]}, \quad (2)$$

where R_o , a , b , and θ_c are fitting parameters. By symmetry, the same functions, with θ_c shifted by $2\pi/3$ and $4\pi/3$, were used to fit the data at higher θ values. [Note that although the form of Eq. (2) provides an analytical means to calculate $\dot{R}(\theta)$ and $\ddot{R}(\theta)$, the first and the second spatial derivatives of R with respect to θ , it has no physical significance.] The solid line in Fig. 5(b) is the analytical fit obtained using Eq. (2).

The inverse Legendre transform of $R(\theta)$ yields *relative* values of $\beta(\varphi)$ through the relationship^{17,18}

$$\beta(\varphi) = \lambda \frac{[R(\theta)]^2}{\{[R(\theta)]^2 + [\dot{R}(\theta)]^2\}^{1/2}} \quad (3a)$$

where φ is the local normal to the equilibrium shape R at θ and is defined as¹⁵

$$\varphi(\theta) = \theta - \arctan\left[\frac{\dot{R}(\theta)}{R(\theta)}\right]. \quad (3b)$$

The proportionality constant λ in Eq. (3a) is the equilibrium chemical potential of the island per unit area. Equations (3a) and (3b) offer an analytical approach for computing relative $\beta(\varphi)$ values. This method eliminates the conventional geometric construction of the inverse Wulff plot, which involves the tedious procedure of drawing normal vectors from the center of mass of the island to the tangent lines at every point along $R(\theta)$, the envelope of which yields $\beta(\varphi)$.

Fits to the equilibrium shape $R(\theta)$ using Eq. (2) yield $\varphi(\theta)$ and relative $\beta(\varphi)$ values directly from Eqs. (3a) and (3b). Polar plots of $\beta(\varphi)$ (dotted line), with $\lambda = 1$, and $R(\theta)$ (solid line) for the vacancy island in Fig. 4(b) are shown in Fig. 6. The two alternating $\langle 110 \rangle$ steps are labeled as S_1 and S_2 and the corresponding radial distances from the center of the island are R_1 and R_2 , respectively. The β_1/β_2 step energy ratio (i.e., the maximum variation of β with φ) is 0.72. β_1/β_2 values determined from the measured equilibrium shapes $R(\theta)$ using Eq. (3a) are plotted for all adatom and

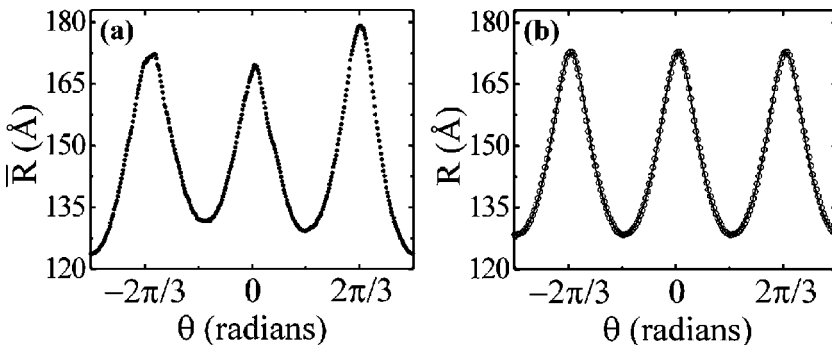


FIG. 5. Plots of (a) average island shape \bar{R} and (b) equilibrium shape R vs θ for the vacancy island shown in Fig. 4(b). The open circles are the measured data while the solid line in (b) is fit with Eq. (2).

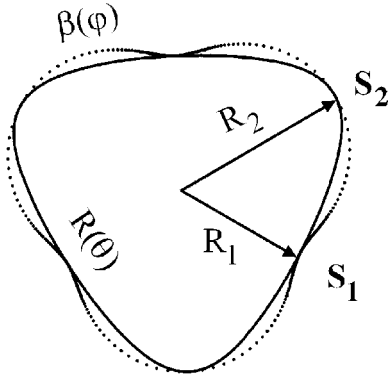


FIG. 6. Polar plots of $R(\theta)$ (solid line) and relative $\beta(\varphi)$ values (dotted line) determined using Eq. (3a) with $\lambda = 1$ and Eq. (3b). The two $\langle 110 \rangle$ close-packed steps bounding the island are labeled S_1 and S_2 while the corresponding radial distances from the center of the island are R_1 and R_2 , respectively.

vacancy islands as a function of R_{avg} , where $R_{\text{avg}} \equiv \sqrt{A/\pi}$ is the orientation-averaged radius of an island with area A , and temperature T_a in Figs. 7(a) and 7(b), respectively. The results show that size- ($R_{\text{avg}} = 50\text{--}260 \text{ \AA}$) and temperature- ($T_a = 1165\text{--}1248 \text{ K}$) dependent changes in β_1/β_2 are $<5\%$ and do not follow any obvious trend.

IV. THERMAL SHAPE FLUCTUATIONS OF ANISOTROPIC TiN(111) ISLANDS

In this section, we analyze temporal fluctuations about equilibrium TiN(111) island shapes using the anisotropic theory of shape fluctuations^{17,18} to determine λ and, hence, *absolute* orientation-dependent $\beta(\varphi)$ values. The amplitude $g(\theta, t_a)$ of the temporal fluctuations in island shape, defined as in Refs. 14 and 15 to be the normalized deviation of the temporal shape $r(\theta, t_a)$ from the time-averaged shape $\bar{R}(\theta)$, is given by the relation

$$g(\theta, t_a) \equiv \frac{[r(\theta, t_a) - \bar{R}(\theta)]}{\bar{R}(\theta)}. \quad (4)$$

The solid line shown in Fig. 8 is a plot of average island shape \bar{R} vs θ for a vacancy island at $T_a = 1165 \text{ K}$. The open circles in Fig. 8 are the measured root-mean-square fluctuations $g_{\text{rms}}(\theta) \equiv \langle [g(\theta, t_a)]^2 \rangle^{1/2}$ of the vacancy island as a function of θ . $g_{\text{rms}}(\theta)$ is clearly orientation dependent. The θ

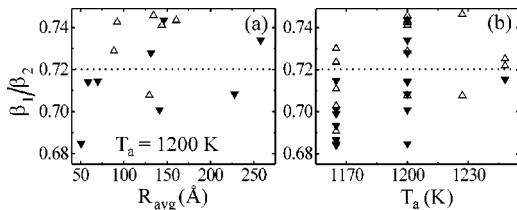


FIG. 7. The ratio β_1/β_2 of S_1 to S_2 step energies is plotted as a function of (a) average island radius R_{avg} at $T_a = 1200 \text{ K}$ and (b) annealing temperature T_a . The open and solid triangles correspond to adatom and vacancy islands, respectively.

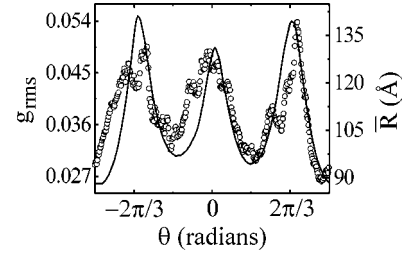


FIG. 8. g_{rms} (open circles) and \bar{R} (solid line) plotted vs θ for a vacancy island at $T_a = 1165 \text{ K}$.

values corresponding to the maxima and minima in g_{rms} coincide, within experimental uncertainties, with those of \bar{R} . This is consistent with the fact that the islands are highly anisotropic. The nearly straight S_1 steps have low curvature with higher stiffnesses and, hence, smaller fluctuation amplitudes than the curved S_2 steps. [For isotropic (circular) islands, where $\beta(\varphi) = \bar{\beta}(\varphi) = \beta_o$ is constant, g_{rms} is orientation independent.] These results provide direct evidence of strong step-edge anisotropy that cannot be accounted for in isotropic shape fluctuation theories.^{14,15}

The time-dependent total free energy $F(t_a)$ of an island is related to the island shape $r(\theta, t_a)$ through the relationship

$$F(t_a) = \int_0^{2\pi} d\theta [\beta[\varphi(\theta, t_a)] \sqrt{[r(\theta, t_a)]^2 + [\dot{r}(\theta, t_a)]^2}] \quad (5)$$

where $\dot{r}(\theta, t_a)$ represents the first spatial derivative of $r(\theta, t_a)$ with respect to θ . The equilibrium shape corresponds to the minimum island free energy F_o . Thus, temporal deviations $g(\theta, t_a)$ about the equilibrium shape result in an increase in the free energy $\Delta F(t_a) \equiv [F(t_a) - F_o]$. Expressing $\beta[\varphi(t_a)]$ and $r(\theta, t_a)$ in Eq. (5) in terms of λ , $R(\theta)$, and $g(\theta, t_a)$, we obtain an expression for $\Delta F(t_a)$ which, upon simplification,¹⁸ can be written as

$$\Delta F(t_a) = \frac{\lambda}{2} \int_0^{2\pi} d\theta \left[\frac{[R(\theta)]^2 [\dot{g}(\theta, t_a)]^2}{\{[R(\theta)]^2 + 2[\dot{R}(\theta)]^2 - [R(\theta)\ddot{R}(\theta)]\}^{1/2}} - [R(\theta)g(\theta, t_a)]^2 \right] \quad (6)$$

$\dot{g}(\theta, t_a)$ in Eq. (6) represents the first spatial derivative of $g(\theta, t_a)$ with respect to θ .

We identify the integrand in Eq. (6) with a fluctuation function $G(\theta, t_a)$ such that

$$G(\theta, t_a) \equiv [\chi(\theta, t_a)]^2 - [\rho(\theta, t_a)]^2, \quad (7)$$

with

$$\chi(\theta, t_a) \equiv \frac{[R(\theta)]^2 [\dot{g}(\theta, t_a)]}{\{[R(\theta)]^2 + 2[\dot{R}(\theta)]^2 - [R(\theta)\ddot{R}(\theta)]\}^{1/2}} \quad (8a)$$

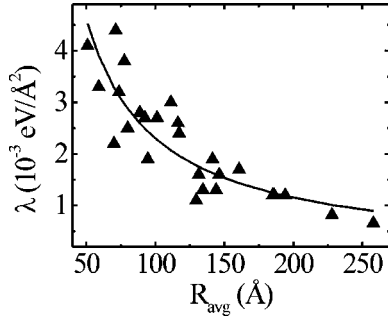


FIG. 9. Plot of λ vs R_{avg} . The solid triangles represent λ results determined using Eq. (10) while the solid line is fit using a function of the form $\lambda = B/R_{\text{avg}}$ with $B = 0.23 \pm 0.01$ eV/Å.

and

$$\rho(\theta, t_a) \equiv g(\theta, t_a) \bar{R}(\theta). \quad (8b)$$

Note that we have used $\bar{R}(\theta)$ in Eq. (8b) since the experimental $g(\theta, t_a)$ data are measured with respect to \bar{R} rather than R . Equation (6) can be rewritten in terms of $G(\theta, t_a)$ as

$$\Delta F(t_a) = \frac{\lambda}{2} \int_0^{2\pi} d\theta G(\theta, t_a). \quad (9)$$

Expressing the functions given in Eqs. (8a) and (8b) as Fourier series $\chi(\theta, t_a) = \sum_n \chi_n(t_a) e^{in\theta}$ and $\rho(\theta, t_a) = \sum_n \rho_n(t_a) e^{in\theta}$ allows Eq. (9) to be written in terms of the Fourier components $\chi_n(t_a)$ and $\rho_n(t_a)$ as $\Delta F(t_a) = \pi \lambda \sum_n G_n(t_a)$, in which $G_n(t_a) \equiv |\chi_n(t_a)|^2 - |\rho_n(t_a)|^2$. From the generalized equipartition theorem,²⁸ the time-averaged free energy $\langle \Delta F(t_a) \rangle$ is equal to $(N_{\text{max}} k_B T_a / 2)$, where N_{max} corresponds to the maximum number of allowable fluctuation modes. Thus, we obtain

$$\lambda = \frac{N_{\text{max}} k_B T_a}{2\pi \sum_n \langle G_n(t_a) \rangle}. \quad (10)$$

The equilibrium chemical potential per unit area λ can, therefore, be obtained from N_{max} and $\langle G_n(t_a) \rangle$. N_{max} is determined from the island size and corresponds to one half of the total number of atoms along the island periphery of a single atomic layer.²⁹ $\langle G_n(t_a) \rangle$ values were determined from the STM measurements of $g(\theta, t_a)$ as described below.

First, $\dot{R}(\theta)$ and $\ddot{R}(\theta)$ were derived analytically from fits to $R(\theta)$ using Eq. (2) and $g(\theta, t_a)$ data determined using Eq. (4). The Fourier modes $g_n(t_a)$ were then extracted from $g(\theta, t_a)$ and $\dot{g}(\theta, t_a)$ values obtained from $g_n(t_a)$ using the relation $\dot{g}(\theta, t_a) = i \sum_n n g_n(t_a) e^{in\theta}$. Finally, $\chi(\theta, t_a)$ and $\rho(\theta, t_a)$ results, computed according to Eqs. (8a) and (8b), were used to calculate the Fourier terms $\langle |\rho_n(t_a)|^2 \rangle$ and $\langle |\chi_n(t_a)|^2 \rangle$, and hence, $\langle G_n(t_a) \rangle$. Substituting N_{max} and $\langle G_n(t_a) \rangle$ values into Eq. (10), we obtained size-dependent λ results for all islands.

Figure 9 is a plot of λ values (solid triangles) vs average island size R_{avg} for all adatom and vacancy islands at all temperatures, $T_a = 1165$ – 1248 K. We have shown previously¹³ that λ can be expressed in terms of a parameter

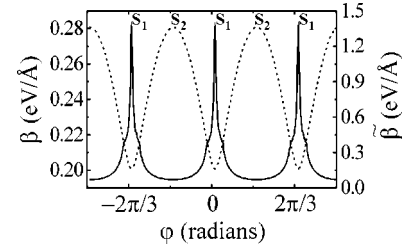


FIG. 10. Absolute values of β vs φ (dashed line) and $\tilde{\beta}$ vs φ (solid line) for a TiN(111) vacancy island at $T_a = 1248$ K.

B , which is independent of step orientation and island size, as $\lambda = B/R_{\text{avg}}$. B determines the energy scale of the surface equilibrium chemical potential. The solid line in Fig. 9, a least-squares fit to the λ vs R_{avg} values, yields $B = 0.23 \pm 0.01$ eV/Å.

V. TiN(111) 2D ISLAND STEP ENERGIES AND STEP STIFFNESSES

Here, we substitute the λ results obtained in the previous section, together with $R(\theta)$ and $\dot{R}(\theta)$, into Eqs. (3a) and (3b) to determine absolute orientation-dependent $\beta(\varphi)$ values. The dashed line in Fig. 10 is a typical plot of β vs φ , in this case for a vacancy island at $T_a = 1248$ K. Averaging over all TiN(111) vacancy islands at all annealing temperatures (1165–1248 K), we obtain step energies β_1 and β_2 for the two $\langle 110 \rangle$ steps of 0.24 ± 0.05 and 0.34 ± 0.08 eV/Å, respectively. Essentially identical values, $\beta_1 = 0.23 \pm 0.04$ and $\beta_2 = 0.31 \pm 0.06$ eV/Å, are obtained for TiN(111) adatom islands.

Step-edge stiffness $\tilde{\beta}(\varphi)$, defined in Eq. (1), can be extracted directly from $\beta(\varphi)$. However, this requires numerical computation of $d^2\beta(\varphi)/d\varphi^2$ from discrete $\beta(\varphi)$ data. Alternatively, $\tilde{\beta}(\varphi)$ can be obtained from λ and the equilibrium island curvature function $\kappa(\theta)$ through the expression¹⁷

$$\tilde{\beta}(\varphi) = \frac{\lambda}{\kappa(\theta)}, \quad (11a)$$

where $\kappa(\theta)$ is given by

$$\kappa(\theta) = \frac{[R(\theta)]^2 + 2[\dot{R}(\theta)]^2 - [R(\theta)\ddot{R}(\theta)]}{\{[R(\theta)]^2 + [\dot{R}(\theta)]^2\}^{3/2}}. \quad (11b)$$

$\kappa(\theta)$ was calculated for all adatom and vacancy islands from the analytical fits to $R(\theta)$ using Eq. (2) to obtain absolute orientation-dependent $\tilde{\beta}$ values. The solid line in Fig. 10 is a representative plot of $\tilde{\beta}$ vs φ , corresponding to the $\beta(\varphi)$ values plotted in Fig. 10, for a vacancy island at $T_a = 1248$ K.³⁰ Averaging over all TiN(111) vacancy islands at all annealing temperatures (1165–1248 K), we obtain step stiffnesses $\tilde{\beta}_1$ and $\tilde{\beta}_2$ of 1.6 ± 0.5 and 0.08 ± 0.01 eV/Å, respectively. Slightly higher results, $\tilde{\beta}_1 = 2.2 \pm 1.5$ with $\tilde{\beta}_2 = 0.09 \pm 0.02$ eV/Å, are obtained for the TiN(111) adatom islands.

TABLE I. Calculated average kink energies and absolute step energies at 0 K for the two $\langle 110 \rangle$ steps on TiN(111).

Parameter	TiN(111)
ε_1 (eV)	0.44 ± 0.05
ε_2 (eV)	0.14 ± 0.02
$\beta_1(0)$ (eV/Å)	0.23 ± 0.05
$\beta_2(0)$ (eV/Å)	0.34 ± 0.07

The larger uncertainties in determining $\tilde{\beta}_1$ arise from the difficulty in determining the curvature of a nearly straight step.

The uncertainty introduced in the determination of step energies due to limited spatial resolution in the fluctuation measurements is of order one-half of a pixel width.¹⁴ Based upon this, we estimate maximum uncertainties in β due to measurement errors in $\rho(\theta, t_a)$ to be $\approx 5\%$. This is less than statistical standard deviations in the results.

Step stiffness is a measure of the step diffusivity and hence controls the meandering of the steps. Assuming single kink excitation, Emundts, Nowicki, and Bonzel¹⁰ derived an expression, based upon Akutsu and Akutsu's hexagonal lattice-gas model,³¹ relating $\tilde{\beta}$ and the kink formation energy ε on a close-packed step as

$$\tilde{\beta} = \frac{2k_B T}{3a_{\parallel}} \left[\exp\left(\frac{\varepsilon}{k_B T}\right) - 4 \exp\left(\frac{-2\varepsilon}{k_B T}\right) \right], \quad (12)$$

where a_{\parallel} is the unit lattice spacing parallel to the step edge. For TiN(111), $a_{\parallel} = 2.99$ Å for both S_1 and S_2 steps. Solving Eq. (12) for ε , using $\tilde{\beta}_1$ and $\tilde{\beta}_2$ values obtained from all 26 islands at $T_a = 1165$ –1248 K, we calculate average kink formation energies: $\varepsilon_1 = 0.44 \pm 0.05$ and $\varepsilon_2 = 0.14 \pm 0.02$ eV. Since kink energies are model dependent, these values should be considered only as estimates with the largest uncertainty of $\approx 25\%$ for the curved S_2 step, where $\varepsilon_2/k_B T \approx 1$.³²

Using the kink and step energy results for the two close-packed steps on TiN(111) islands, we calculate average step energies $\beta(0)$ at $T_a = 0$ K from the relation¹⁰

$$\beta(T) = \beta(0) - \frac{k_B T}{a_{\parallel}} \left[2 \exp\left(\frac{-\varepsilon}{k_B T}\right) - \exp\left(\frac{-2\varepsilon}{k_B T}\right) \right]. \quad (13)$$

This yields $\beta_1(0) = 0.23 \pm 0.05$ and $\beta_2(0) = 0.34 \pm 0.07$ eV/Å. Table I lists the average kink energies and step energies at 0 K for the two $\langle 110 \rangle$ steps on TiN(111). We note that the $\beta(0)$ values are, within experimental uncertainties, equal to the average step energy values obtained from all the islands observed over the temperature range 1165–1248 K. Thus, TiN(111) step energies exhibit only a very weak tem-

perature dependence between 0 and 1248 K. $\beta(0)$ values for the (111) surfaces of fcc Pb (0.037 and 0.033 eV/Å for the two $\langle 110 \rangle$ steps),¹⁰ Cu (0.066 eV/Å),³³ and Ag (0.085 eV/Å) (Ref. 33) are significantly lower. The higher step energies for TiN(111) are reasonable given the fact that the melting point T_m , a measure of the bonding and cohesive energies in a solid, is more than a factor of 2 higher for TiN (Ref. 34) than for Cu, Ag, and Pb due to the mixture of strong covalent and ionic bonds in the nitride.

Finally, we note that the entropic contribution to step energies on metallic surfaces is of order $(k_B T_a / a_{\parallel}) \ln[\coth(\varepsilon / 2k_B T_a)]$ (Ref. 35) and generally ignored.^{9,14} Using $\varepsilon = 0.44$ and 0.14 eV with $T_a = 1200$ K in the above expression, we estimate the corresponding entropic contributions to be $\approx -1.0 \times 10^{-3}$ and $\approx -1.8 \times 10^{-2}$ eV/Å, respectively, which are smaller than the statistical uncertainties (0.04 and 0.06 eV/Å for S_1 and S_2 , respectively).

VI. CONCLUSIONS

In situ STM was used to measure shape fluctuations around the equilibrium shape of 2D TiN(111) adatom and vacancy islands at temperatures between 1165 and 1248 K. TiN(111) islands are highly anisotropic with $\beta_1/\beta_2 = 0.72 \pm 0.02$ at $T_a \approx 1200$ K ($\approx 0.38 T_{m, \text{TiN}}$). Temporal fluctuations about the equilibrium shapes are also strongly orientation dependent with the same threefold symmetry as that of the island. From the STM data and the theory of anisotropic shape fluctuations, we determined absolute orientation-dependent TiN(111) step energies and stiffnesses. For the two $\langle 110 \rangle$ steps, we obtain $\beta_1 = 0.23 \pm 0.05$ and $\tilde{\beta}_1 = 1.9 \pm 1.1$ eV/Å with $\beta_2 = 0.33 \pm 0.07$ and $\tilde{\beta}_2 = 0.08 \pm 0.02$ eV/Å. Corresponding kink energies, $\varepsilon_1 = 0.44 \pm 0.05$ and $\varepsilon_2 = 0.14 \pm 0.02$ eV, were calculated from the step stiffness values. Estimated step energy values at 0 K are $\beta_1(0) = 0.23 \pm 0.05$ and $\beta_2(0) = 0.34 \pm 0.07$ eV/Å indicating that TiN(111) step energies exhibit only a very weak temperature dependence between 0 K and the maximum measurement temperature, 1248 K.

ACKNOWLEDGMENTS

The authors gratefully acknowledge the financial support of the U.S. Department of Energy under Contract No. DEEG02-91ER45439 and the NSF focused research group at the Materials Computation Center under Contract No. DMR-9976550. S.K. is partially supported by the University of Illinois Critical Research Initiative program (Contract No. CRI00HSIA). We also appreciate the use of the facilities at the Center for Microanalysis of Materials, partially supported by the DOE, at the University of Illinois.

¹F. H. Baumann, D. L. Chopp, T. Díaz de la Rubia, G. H. Gilmer, J. E. Greene, H. Huang, S. Kodambaka, P. O'Sullivan, and I. Petrov, MRS Bull. **26**, 182 (2001).

²S. Kodambaka, V. Petrova, A. Vailionis, P. Desjardins, D. G. Ca-

hill, I. Petrov, and J. E. Greene, Surf. Rev. Lett. **7**, 589 (2000); Thin Solid Films **392**, 164 (2001).

³W. W. Mullins, Interface Sci. **9**, 9 (2001).

⁴M. Giesen, Prog. Surf. Sci. **68**, 1 (2001), and references therein.

- ⁵M. Wortis, in *Chemistry and Physics of Solid Surfaces VII*, edited by R. Vanselow and R. F. Howe (Springer, New York, 1988), p. 367; H. van Beijeren and I. Nolden, in *Topics in Current Physics* (Springer, Berlin, 1987), Vol. 43, p. 259.
- ⁶P. Nozières, in *Solids Far From Equilibrium*, edited by C. Godrèche (Cambridge University, Cambridge, England, 1992), p. 1.
- ⁷N. C. Bartelt, R. M. Tromp, and E. D. Williams, *Phys. Rev. Lett.* **73**, 1656 (1994); N. C. Bartelt and R. M. Tromp, *Phys. Rev. B* **54**, 11 731 (1996).
- ⁸K. Arenhold, S. Surnev, H. P. Bonzel, and P. Wynblatt, *Surf. Sci.* **424**, 271 (1999); H. P. Bonzel and A. Emundts, *Phys. Rev. Lett.* **84**, 5804 (2000).
- ⁹G. S. Icking-Konert, M. Giesen, and H. Ibach, *Phys. Rev. Lett.* **83**, 3880 (1999).
- ¹⁰A. Emundts, M. Nowicki, and H. P. Bonzel, *Surf. Sci.* **496**, L35 (2002).
- ¹¹K. Morgenstern, G. Rosenfeld, and G. Comsa, *Phys. Rev. Lett.* **76**, 2113 (1996); K. Morgenstern, G. Rosenfeld, E. Lægsgaard, F. Besenbacher, and G. Comsa, *ibid.* **80**, 556 (1998).
- ¹²G. S. Icking-Konert, M. Giesen, and H. Ibach, *Surf. Sci.* **398**, 37 (1998).
- ¹³S. Kodambaka, S. V. Khare, V. Petrova, A. Vailionis, I. Petrov, and J. E. Greene, *Surf. Sci.* **513**, 468 (2002).
- ¹⁴D. C. Schlößer, L. K. Verheij, G. Rosenfeld, and G. Comsa, *Phys. Rev. Lett.* **82**, 3843 (1999).
- ¹⁵S. V. Khare and T. L. Einstein, *Phys. Rev. B* **54**, 11 752 (1996).
- ¹⁶C. Steimer, M. Giesen, L. Verheij, and H. Ibach, *Phys. Rev. B* **64**, 085416 (2001).
- ¹⁷S. Kodambaka, V. Petrova, S. V. Khare, D. D. Johnson, I. Petrov, and J. E. Greene, *Phys. Rev. Lett.* **88**, 146101 (2002).
- ¹⁸S. V. Khare, S. Kodambaka, D. D. Johnson, I. Petrov, and J. E. Greene, *Surf. Sci.* **522**, 75 (2003).
- ¹⁹I. Petrov, F. Adibi, J. E. Greene, W. D. Sproul, and W.-D. Münz, *J. Vac. Sci. Technol. A* **10**, 3283 (1992).
- ²⁰J. E. Greene, J.-E. Sundgren, L. Hultman, I. Petrov, and D. B. Bergstrom, *Appl. Phys. Lett.* **67**, 2928 (1995).
- ²¹R. L. Doolittle, *Nucl. Instrum. Methods Phys. Res. B* **9**, 344 (1985).
- ²²K. Zeng and R. Schmid-Fetzer, *Z. Metallkd.* **87**, 540 (1996).
- ²³Inorganic Index to Powder Diffraction File (Joint Committee on Powder Diffraction Standards, Pennsylvania, 1997): Card numbers 38-1420 and 08-0117 for TiN and TiO, respectively.
- ²⁴The 111 direction in the *B1*-NaCl structure of TiN is polar, consisting of alternating layers of Ti and N atoms.
- ²⁵M. Marlo and V. Milman, *Phys. Rev. B* **62**, 2899 (2000); D. Gall, S. Kodambaka, M. A. Wall, I. Petrov, and J. E. Greene (unpublished).
- ²⁶Steve Barrett, Computer code IMAGE SXM, (Surface Science Research Centre, Liverpool, England, 2000), <http://reg.ssci.liv.ac.uk>
- ²⁷H.-C. Jeong and E. D. Williams, *Surf. Sci. Rep.* **34**, 171 (1999).
- ²⁸K. Huang, in *Statistical Mechanics* (Wiley, New York, 1963), p. 149.
- ²⁹Since each TiN(111) island consists of alternating atomic Ti and N layers with equal numbers of atoms, the number N of boundary atoms in each atomic layer is equal, i.e., $N_{\text{Ti}} = N_{\text{N}}$. Thus, $N_{\text{max}} = N_{\text{Ti}}/2$.
- ³⁰Lorentzian fits, given by Eq. (2), yield smooth fits to all the data near maxima and minima of R . However, there exists two points of discontinuity at intermediate R values that result in erroneous spatial derivatives. These values were manually corrected to obtain a smooth curvature function $\kappa(\theta)$.
- ³¹N. Akutsu and Y. Akutsu, *J. Phys.: Condens. Matter* **11**, 6635 (1999).
- ³²P. J. Feibelman, *Phys. Rev. B* **62**, 17 020 (2000).
- ³³M. Giesen, C. Steimer, and H. Ibach, *Surf. Sci.* **471**, 80 (2001).
- ³⁴*CRC Handbook of Chemistry and Physics*, 82nd ed. (Chemical Rubber, Boca Raton, 2001), pp. 4–91.
- ³⁵E. D. Williams, R. J. Phaneuf, J. Wei, N. C. Bartelt, and T. L. Einstein, *Surf. Sci.* **294**, 219 (1993).